

Solution-Processed $\text{In}_2\text{O}_3/\text{ZnO}$ Heterojunction Electron Transport Layers for Efficient Organic Bulk Heterojunction and Inorganic Colloidal Quantum-Dot Solar Cells

Flurin Eisner, Akmaral Seitkhan, Yang Han, Dongyoon Khim, Emre Yengel, Ahmad R. Kirmani, Jixian Xu, F. Pelayo García de Arquer, Edward H. Sargent, Aram Amassian, Zhuping Fei, Martin Heeney, and Thomas D. Anthopoulos*

We report the development of a solution-processed $\text{In}_2\text{O}_3/\text{ZnO}$ heterojunction electron transport layer (ETL) and its application in high efficiency organic bulk-heterojunction (BHJ) and inorganic colloidal quantum dot (CQD) solar cells. Study of the electrical properties of this low-dimensional oxide heterostructure via field-effect measurements reveals that electron transport along the heterointerface is enhanced by more than a tenfold when compared to the individual single-layer oxides. Use of the heterojunction as the ETL in organic BHJ photovoltaics is found to consistently improve the cell's performance due to the smoothening of the ZnO surface, increased electron mobility and a noticeable reduction in the cathode's work function, leading to a decrease in the cells' series resistance and a higher fill factor (FF). Specifically, non-fullerene based organic BHJ solar cells based on $\text{In}_2\text{O}_3/\text{ZnO}$ ETLs exhibit very high power conversion efficiencies (PCE) of up to 12.8%, and high FFs of over 70%. The bilayer ETL concept is further extended to inorganic lead-sulphide CQD solar cells. Resulting devices exhibit excellent performance with a maximum PCE of 8.2% and a FF of 56.8%. The present results highlight the potential of multilayer oxides as novel ETL systems and lay the foundation for future developments.

1. Introduction

Solar cells based on organic light absorbing materials have been extensively studied because of their potential for cost-effective and high-throughput fabrication on flexible modules.^[1–3] Thanks to careful engineering of the active (i.e., light absorbing) layer of so-called organic bulk-heterojunction (BHJ) solar cells, the power-conversion efficiency (PCE) of such cells has recently reached over 11% with cells employing fullerene derivatives,^[4–6] and over 13% with polymer:small molecule blends.^[7–9] In addition to the active materials, there has also been recent progress in the study of interfacial layers, or interlayers, which are inserted between the active layers and the electrodes (i.e., anode and cathode).^[5,10–17] The presence of these interlayers is vital to improve charge selectivity at the electrodes, and ensure a good (Ohmic) electrical contact at the electrodes, and have been shown to be essential for high performing

organic,^[18–20] inorganic,^[21] and hybrid organic–inorganic^[22] solar cells. In the conventional organic BHJ solar cell architecture, where the transparent conductive electrode (usually ITO) acts as the anode, the most common bottom-layer interfacial layers are PEDOT:PSS^[23,24] and CuSCN.^[6,11,12] However, there has been a recent move to the so-called “inverted” n-i-p structure, where the ITO side of the device acts as the cathode terminal, due to the improved stability and advantages for roll-to-roll fabrication of this architecture over the “conventional” structure.^[25,26]


In inverted organic BHJ solar cell, the bottom ETL is usually a metal oxide, and most often zinc oxide (ZnO).^[15,27,28] The benefits of ZnO include its excellent electron transport properties, good ambient stability, and its easy solution processability to form smooth and well defined layers^[13]; several solution processing techniques for ZnO are possible, the most popular among which are using the sol-gel method from a zinc acetate precursor,^[15,28] and by deposition from an aqueous

F. Eisner, Dr. D. Khim, Prof. T. D. Anthopoulos
Department of Physics
The Centre for Plastic Electronics
Imperial College London, London SW7 2AZ, UK

A. Seitkhan, Dr. E. Yengel, Dr. A. R. Kirmani, Prof. A. Amassian,
Prof. T. D. Anthopoulos
Division of Physical Sciences and Engineering and KAUST Solar Centre
King Abdullah University of Science and Technology (KAUST)
Thuwal 23955-6900, Saudi Arabia
E-mail: thomas.anthopoulos@kaust.edu.sa

Dr. Z. Fei, Dr. Y. Han, Prof. M. Heeney
Department of Chemistry
The Centre for Plastic Electronics
Imperial College London, London SW7 2AZ, UK

Dr. Jixian Xu, Dr. F. P. García de Arquer, Prof. E. H. Sargent
Department of Electrical and Computer Engineering
University of Toronto, Toronto, Ontario M5S 3G4, Canada

 The ORCID identification number(s) for the author(s) of this article can be found under <https://doi.org/10.1002/solr.201800076>.

DOI: 10.1002/solr.201800076

solution of an amine-zinc complex.^[29,30] Because of its versatility and popularity, various methods to improve the performance of ZnO-based electron contacts have been investigated. One method has been to *n*-dope the ZnO with a variety of metals and organics in order to improve the electron mobility, and to achieve a preferable energy alignment with the active layer in order to improve electron injection to the acceptor. Commonly used dopants are metals such as aluminium,^[31–35] tin,^[36] and lithium,^[16] but organic dopants have also been used to good effect.^[37] A second method has been to apply an additional organic interfacial layer between the ZnO and the active layer in order to achieve a larger built-in potential and enhanced electron transfer from the acceptor.^[38–42] To this end, interlayers such as polyethylenimine ethoxylated (PEIE), polyethylenimine (PEI), and poly(2-ethyl-2-oxazoline) (PeOz) nanodots have all been shown to be very effective in increasing the PCE of BHJ-based organic photovoltaics (OPVs).^[17,43–47]

In this contribution, we expand on the concept of improving the performance of ZnO based polymer BHJ as well as colloidal quantum dot (CQD) solar cells by introducing an additional, extremely thin, indium oxide (In₂O₃) layer in between the cathode (ITO) and the ZnO film. The resulting bilayer architecture has recently been shown to lead to dramatic improvements in the electron mobility of TFTs, achieving field-effect mobilities of up to 45 cm²/Vs due to synergistic effects of an extremely chemically sharp In₂O₃/ZnO interface and the presence of a two-dimensionally (2D) confined electron cloud at the interface.^[30,48–51] The use of such a bilayer structure has also briefly been previously reported in our group in organic BHJ solar cells with copper iodide (CuI) as the hole transporting layer (HTL),^[52] as well as more recently in high efficiency BHJ OPVs,^[8] but has not been studied in detail. In this work, we show that use of a similar oxide bilayer structure allows for the growth of extremely smooth ETLs with enhanced electron mobility and tuneable Fermi energy. When incorporated in both fullerene and non-fullerene based BHJ OPVs, resulting devices exhibit reduced series resistance and significantly enhanced PCE values. Finally, we demonstrate the universal nature of the multilayer ETL concept by implementing it on inorganic lead-sulphide (PbS) CQD solar cells, for which we obtain PCE values that are comparable to those from devices based on standard thick (typically >100 nm) single-layer ZnO ETLs.

2. Electron Transport in Bilayer In₂O₃/ZnO ETLs

The most common route for depositing good quality and uniform ZnO layers for organic solar cell is via a sol-gel method from a zinc acetate precursor. The downside of this process is the requirement for high annealing temperatures (≥ 200 °C), which is often incompatible with inexpensive flexible plastic substrates, to achieve good enough transport to avoid large series resistances in solar cells, and the need for highly toxic solvents to dissolve the precursor.^[27] In contrast, zinc oxide thin films obtained by the spin coating of a zinc oxide-amine complex in an aqueous solution have been popular for transistor applications, due to the ability for this method to result in highly polycrystalline and ultra-thin (<10 nm) layers which achieve

higher mobilities at annealing temperatures below 180 °C than those achieved with the sol-gel method. In order to demonstrate the versatility of the approach used here, layers of ZnO grown from both methods were investigated. From here on we denote ZnO obtained via the sol-gel method as ZnO (s-g), and ZnO layers obtained via the aqueous route as ZnO (aq).

The charge transport properties of ZnO(s-g) and ZnO(aq) were investigated using field-effect transistor measurements employing a bottom-gate, top-contact (BG-TC) architecture (inset, **Figure 1**). The transfer characteristics, source-drain (S-D) current (I_D) versus gate voltage (V_G), of the transistors were measured both in the saturation ($V_D = 30$ V) and in the linear ($V_D = 10$ V) operating regimes. The extracted mobility values are summarized in **Table 1**, while representative transfer curves of the transistors in the saturation regime are shown in Figure 1. As anticipated, the electron saturation mobility (μ_{sat}) of ZnO(aq) is close to 1 cm²/Vs, roughly two orders of magnitude higher than the mobility of ZnO(s-g). Following the procedure developed in our laboratory,^[14,51] we then proceeded to fabricate In₂O₃/ZnO bilayer transistors. As expected, heterojunction channel TFTs with ZnO(aq) results in a substantial increase in the electron mobility to around 5 cm² V⁻¹ s⁻¹ and, interestingly, a more than 1000 time increase in the mobility of ZnO (s-g) to a similar value (Table 1). Both mobility values are significantly higher than achieved for the single layer In₂O₃ reference transistor, also shown in Figure 1, denoting that the improvement in electron transport comes from the interaction between the ZnO and In₂O₃, rather than the conventional channel formed at the SiO₂/In₂O₃ interface.

3. Morphological Characterization of Bilayer In₂O₃/ZnO ETLs

Having established the positive effect of a bilayer In₂O₃/ZnO structure on the in-plane electron transport in TFTs, we proceeded to examine the possibility of using a similar bilayer

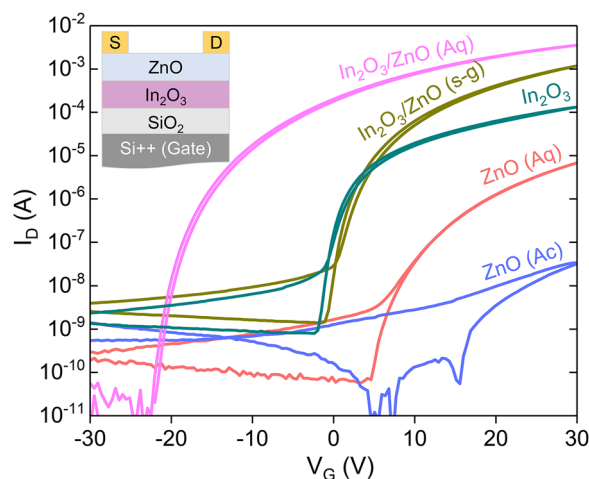


Figure 1. Transfer characteristics of ZnO and In₂O₃/ZnO transistors processed via the aqueous [ZnO(aq)] and sol-gel [ZnO(s-g)] methods. Inset: A schematic of the BG-TC transistor architecture employed. The channel length and width for all devices fabricated were identical and equal to 40 and 1000 μm, respectively.

Table 1. Summary of operating parameters of single layer and bilayer metal oxide BG-TC transistors extracted from at least five devices.

ETL material	μ_{lin} [$\text{cm}^2 \text{V}^{-1} \text{s}^{-1}$]	μ_{sat} [$\text{cm}^2 \text{V}^{-1} \text{s}^{-1}$]	V_{th} [V]
ZnO(aq)	0.4 (± 0.1)	0.55 (± 0.1)	12 (± 0.1)
ZnO(s-g)	0.0012 (± 0.001)	0.0025 (± 0.001)	13 (± 5.3)
In_2O_3	0.8 (± 0.7)	0.9 (± 0.7)	-1 (± 2.6)
$\text{In}_2\text{O}_3/\text{ZnO}$ (aq)	4.2 (± 2.2)	4.8 (± 2.2)	-8 (± 5.4)
$\text{In}_2\text{O}_3/\text{ZnO}$ (s-g)	4.6 (± 1.4)	3.9 (± 1.7)	5 (± 1.2)

The standard deviation of the mean values is given in brackets.

structure as the ETL in BHJ OPVs. It is important to note that an improvement in the in-plane electron mobility found in TFT measurements may not necessary lead to an increase mobility in the vertical direction relevant to solar cells. Nevertheless, the electron accumulation at the heterointerface would most certainly increase the conductivity of the ETL significantly enough to warrant further investigation for solar cell applications. Additionally, whereas in the case of TFTs the oxide bilayer was deposited onto ultra-smooth SiO_2 substrates (<0.1 nm root mean squared (rms) roughness), which allows for the deposition of ultra-thin and extremely smooth layers of In_2O_3 and ZnO,^[14] the indium tin oxide (ITO) substrates used in BHJ OPVs have a much rougher surface (rms in the range 2–5 nm).

To investigate the feasibility of growing such bilayers on ITO, the microstructure of the $\text{In}_2\text{O}_3/\text{ZnO}$ (s-g) bilayer deposited on ITO-patterned glass substrates was studied via cross-sectional high-resolution transmission electron microscopy (HRTEM). As shown by **Figure 2a**, at low magnification only the ITO and ZnO layers can be distinguished, which can be explained by the very similar crystallographic parameters of the ITO and In_2O_3 . To this end, it has been shown by Thirumoorthi et al. that indium oxide upon doping with tin crystallizes in a cubic structure, while *d*-spacing and lattice constants change only slightly due to Sn-atom substitution into In-O lattice.^[53] Therefore, direct detection of the In_2O_3 layer by TEM is expected to be a rather challenging task, especially in the case of a few nm-thin layers.

Despite the challenge, the HRTEM image shown in **Figure 2b** reveals the presence of an apparent interface between ITO/ In_2O_3 and the top ZnO layer. Additional HRTEM images taken above and below this apparent heterointerface verify the existence of the different oxides while providing additional insights. For example, the top ZnO layer appears to be polycrystalline with the lattice spacing of 0.28 nm corresponding to the (100) plane. This was further verified by Fast Fourier Transform (FFT) analysis and by the presence of the additional orientations along the (011) and ($\bar{1}22$). On the other hand, the HRTEM image taken from the bulk ITO layer located below the heterointerface in **Figure 2b** yields the expected *d*-spacing of 0.41 nm which corresponds to the (211) plane with the (400) and (022) planes also appearing on the corresponding FFT pattern (ITO).

In an effort to better understand the chemistry of the heterointerface, we have taken the HRTEM shown in **Figure 2c** and performed energy-dispersive X-ray (EDX) spectroscopy measurements (**Figure S1**, Supporting Information). As evident by the evolution of the EDX signal, the

measured intensity associated with the presence of tin (Sn) drops *ca.* 5 nm earlier than the signal associated with indium (In) when scanning from the bulk of ITO layer toward the top ZnO layer (arrow direction in **Figure S1b**, Supporting Information). This finding is in agreement with the HRTEM image in **Figure 2c** which indicates a thickness for the In_2O_3 layer in the range of 2–4 nm. Furthermore, this apparent In_2O_3 layer is characterized by a high microstructural order potentially as a result of the epitaxial growth on the ITO layer. The small difference observed between EDX signal offsets and the thickness extracted from the HRTEM image can be explained by the EDX scan resolution limit and the signal collection step size of 0.96 nm. Despite the small discrepancies, these measurements provide direct evidence for the existence of a layer containing significantly less tin than the underlying ITO layer (**Figure S1**, Supporting Information). It is thus perfectly reasonable to associate this layer with the existence of an ultra-thin In_2O_3 layer.

In order to investigate the impact that this extremely thin In_2O_3 layer has on the surface morphology of the ZnO deposited on top, the surface topography of all samples studied was investigated via high resolution atomic force microscopy (AFM). **Figure 3a** shows the AFM images (1 μm by 1 μm in size) for all layers including those of bare ITO, and In_2O_3 deposited on ITO (ITO/ In_2O_3), for reference. While both ZnO(aq) and ZnO(s-g) deposited on ITO (ITO/ZnO) are found to form uniform and polycrystalline, there appears to be no major difference in the surface topography between ITO/ZnO and the bilayer ETL systems (i.e., ITO/ $\text{In}_2\text{O}_3/\text{ZnO}$ (aq) and ITO/ $\text{In}_2\text{O}_3/\text{ZnO}$ (s-g)) with the surface of ZnO appearing uniform and independent of the precursor chemistry used.

Further information on the topographical characteristics of the different layers was obtained by comparing the height histograms (**Figure 3b**) for each sample extracted from the AFM data in **Figure 3a**. The first important observation is the smoothing of the ITO surface upon In_2O_3 deposition indicated by a shift of the height distribution toward lower values and a reduction in the RMS surface roughness from 3.03 to 1.79 nm. This, in turn, appears to lead to a smoother ZnO layer when spin cast onto the ITO/ In_2O_3 as opposed to bare ITO, with the RMS roughness decreasing further from 1.33 to 1.14 nm for ZnO (s-g), and from 3.47 to 2.79 nm for ZnO (aq). These are important findings since the roughness of the ZnO cathode layer has previously been directly correlated to the performance of BHJ OPV cells, with smoother ZnO ETL layers yielding cells with consistently lower series resistance, and increased fill factor.^[54,55] Finally, the optical transmission characteristics of the different ETL systems were also measured in the region of 300–900 nm (**Figure S2**, Supporting Information). It is found that both heterojunction ETLs show no significant degradation in their optical transmittance characteristics with their properties determined primarily by the underlying ITO layer.

4. Work Function Engineering in Bilayer $\text{In}_2\text{O}_3/\text{ZnO}$ ETLs

It is well established that the work function of the ETL in an BHJ OPV device plays an important role as it affects the maximum

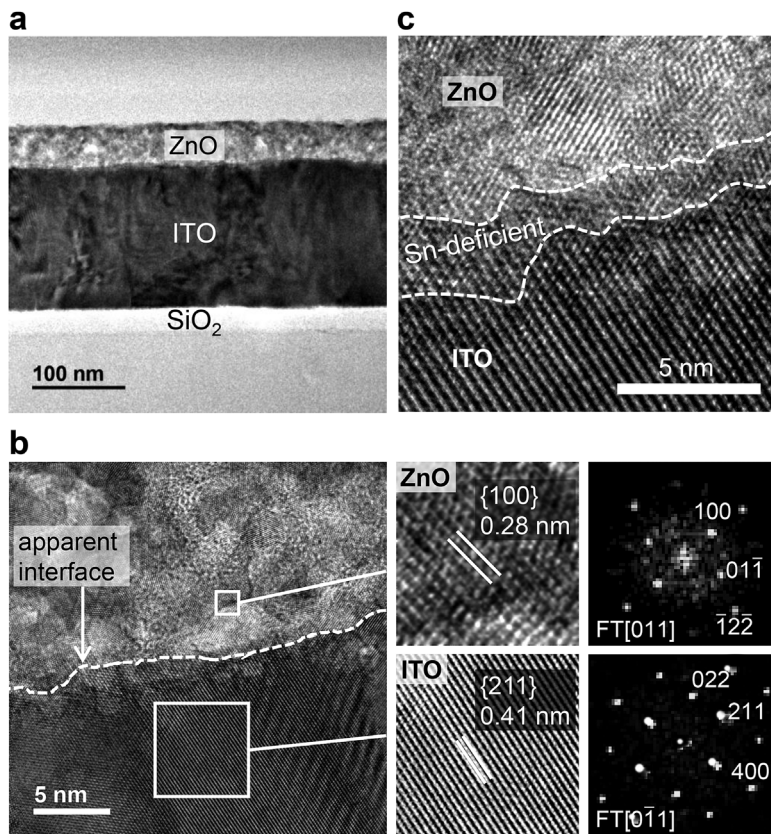


Figure 2. a) Transmission electron microscopy (TEM) images of a $\text{In}_2\text{O}_3/\text{ZnO}$ (s-g) bilayer spin cast on ITO. b) HRTEM image showing the areas at which the FFT patterns were taken across the apparent heterointerface. The lattice spacings of ZnO and ITO corresponding to the expected (100) and (211) planes, respectively, are also indicated. c) Cross-sectional HRTEM image of the ITO/ $\text{In}_2\text{O}_3/\text{ZnO}$ interface, with the Sn-deficient region corresponding to the In_2O_3 layer being highlighted by the dashed line.

achievable open circuit voltage (V_{OC}). This is primarily due to its influence on the electron extraction and contact resistance present between the anode and the active layer, and may therefore have an impact on the short circuit current (J_{SC}) and fill factor (FF) of the device.^[18] To this end, it has been shown that small changes in the work function of the interlayer can have a significant effect on the device built-in voltage (V_{bi}).^[5] To better understand the relation between the cathode's work function and the cell's performance, Kelvin Probe (KP) measurements were performed on all solution processed metal oxide-based ETLs studied.

Figure 4 displays the measured work function for each metal oxide system together with that of ITO for comparison. Here, single layer oxide ETLs refer to ZnO systems deposited on top of the pre-patterned ITO electrodes, while bilayer ETL to ZnO processed onto ITO/ In_2O_3 . Although deposition of In_2O_3 on ITO results in a minimal work function change (<0.1 eV), growth of a ZnO layer onto ITO, either via the sol-gel or the aqueous precursor route, leads to clear reduction in the cathode's work function. The small difference in the work function seen between ZnO(s-q) and ZnO(aq) is most likely attributed to differences in their stoichiometry, a result of the

two different processing routes adopted (i.e., s-g and aq). A further reduction in the work function (by >0.1 eV) is measured when the In_2O_3 layer is inserted between ITO and ZnO. Since the impact of the In_2O_3 layer on ITO's work function is minimal (<0.1 eV), the latter observation is attributed to the electron transfer from the conduction band minimum of ZnO to that of In_2O_3 upon physical contact.^[56] The presence of the sharp chemical interface seen in Figure 2 rules out the impact of material intermixing (alloying), hence making electron transfer the most likely process. Irrespective of the underlying mechanism responsible for the work function increase, these results demonstrate that precise tuning of the cathode's conductivity and work function can be achieved through the use of carefully engineered multilayer oxide ETL structures.

5. PTB7-Th:PCBM Bulk Heterojunction Solar Cells Base on Bilayer ETLs

In order to investigate the potential of bilayer oxide ETLs for application in BHJ OPVs, bulk-heterojunction (BHJ) cells were fabricated using the high efficiency polymer-fullerene blend poly[4,8-bis(5-(2-ethylhexyl)thiophen-2-yl)benzo[1,2-*b*:4,5-*b'*]dithiophene-2,6-diyl-alt-(4-(2-ethylhexyl)-3-fluorothieno[3,4-*b*]thiophene-2-carboxylate-2,6-diyl)] (PTB7-Th)^[57]: [6,6]-phenyl-C71-butyric acid methyl ester (PC₇₁BM)^[58] in an inverted device architecture (**Figure 5a**). The optimum In_2O_3 layer thickness for such cells was found to be in the region of 2–4 nm and was deposited at 6000 rpm in air from a 20 mg mL⁻¹ precursor solution (see Section 8 and Figure S3,

Supporting Information). Thicker In_2O_3 layers were found to adversely affect the cell's performance when compared to the reference single-layer ZnO ETL-based devices. We attribute this to higher thickness of the In_2O_3 layer which gives rise to an energetic barrier between the In_2O_3 and the ZnO.^[56]

Figure 5b shows the current density-voltage (J - V) characteristics for optimized single layer and heterojunction ETLs based solar cells using ZnO(aq) and ZnO(s-g) measured under simulated solar illumination (AM1.5G, 1 sun). The mean values of the various device parameters extracted from 15 individual cells are summarized in **Table 2**. In both cases, cells based on bilayer ETLs perform consistently better than those based on single layer ETLs, with the improvement most notable in the FF, which increase from an average of 63% to 67% for ZnO(aq) and from 64% to 66% for ZnO(s-g)-based devices, respectively. This improvement is also reflected in the decrease of the series resistances (R_s) of the cells (**Figure 5c**), extracted both from the J - V characteristics measured in the dark (**Figure 5d**) and under illumination (**Figure 5b**). The improved FF and lower R_s , is also mirrored, to an extent, by a small increase in the short circuit current (J_{SC}) of the devices, a finding confirmed independently by EQE measurements (**Figure S4**, Supporting Information).

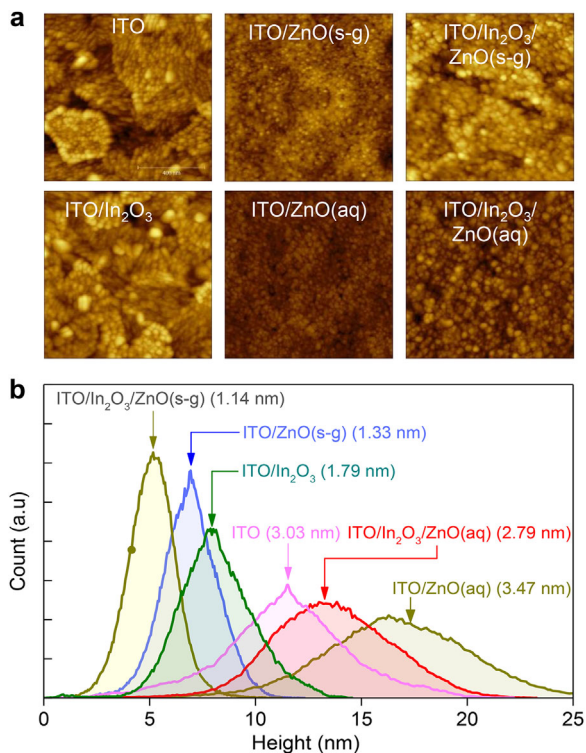


Figure 3. a) Atomic force microscopy (AFM) images of the surface topography of various samples investigated namely; ITO, ITO/In₂O₃, ITO/ZnO(s-g), ITO/ZnO(aq), ITO/In₂O₃/ZnO(s-g), and ITO/In₂O₃/ZnO(aq). The size of each image is the same and equal to 1 μm by 1 μm , while the maximum height in all images is adjusted to 14.7 nm, with lighter regions corresponding to higher values. b) Height histograms extracted from the AFM images in (a) with the numbers in brackets indicating the calculated surface roughness rms value for each sample.

Interestingly, the bilayer ETL appears to have only a small effect on the V_{OC} of the ZnO(s-g) based devices, increasing it by less than 0.01 V, and no noticeable effect on the V_{OC} of the ZnO(aq) devices, suggesting that the V_{OC} in this case is not limited by the workfunction of the ETL. The higher V_{OC} of ZnO(aq) compared to ZnO(s-g) can be attributed to its lower thickness (10–15 nm)

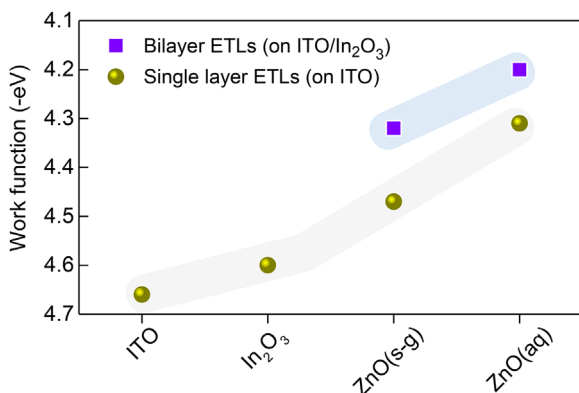


Figure 4. Work function of the various metal oxide layers deposited on ITO determined via Kelvin Probe measurements in dry air. The work function of bare ITO is also shown for comparison.

compared to 30–35 nm) leading to a lower electrical resistance; the saturation of the V_{OC} between ZnO(aq) and In₂O₃/ZnO(aq) in turn suggests that the V_{OC} is limited by other energy levels, that is, HOMO/LUMO offset of PTB7-Th and PC₇₀BM. The relatively large increase in the FF compared to relatively small increase in the J_{SC} , along with the absence of any improvement in the R_{Sh} but large decreases in the R_s , suggests that “smoothing” of the ETL’s surface play a more critical role in enhancing the PCE than electronic effects from changes in its work function. The maximum achieved PCE for the best performing cell using the bilayer In₂O₃/ZnO ETL was 10% for ZnO(s-g) and 10.32% for ZnO(aq), compared to 9% and 9.72%, respectively, for the single layer ETL cells.

The applicability of the bilayer ETL system to other donor-acceptor organic system, has also been investigated. Since the choice of ETL affects mainly the charge transport from the acceptor component to the cathode electrode, various blends with different acceptors were chosen, including the regioregular poly(3-hexylthiophene):indene-C₆₀ bisadduct (P3HT:ICBA), and the high performance fullerene-free systems PBDB-T^[59] blended with the acceptor molecule ITIC,^[60] and PFBDB-T:8C-ITIC,^[8] (Figure 6a).

Figure 6b displays a collection of J - V characteristics measured for the various organic BHJ cells including that for PTB7-Th:PC₇₀BM for comparison. The EQE spectra of each cell are also shown in Figure 6c. Since the energetics of each material system are different (Figure S5, Supporting Information), the impact of changing the ETL is also expected to differ. Figure 6d compares the extracted operating parameters for each blend (averaged over 15 devices or more) between the single and bilayer oxide ETL. In accordance with the results obtained from the PTB7-Th:PC₇₀BM-based cells, incorporation of the bilayer ETL also has a significant positive effect on the series resistance of all other blends, which in turn translates into improvements in the FF in the cases of P3HT:ICBA (from 0.59 to 0.63) and PBDB-T:ITIC (0.62 to 0.64). For the highest performance PFBDB-T:8C-ITIC blend the already high FF of 0.71 remains unaffected, but an increase in the J_{SC} from a mean value of 18.1 to 18.7 mA cm^{-2} is observed, leading to a high mean PCE of 12.3 (± 0.4)% (Table 3). Additionally, a hero cell of 12.8% was obtained using this blend and the bilayer ETL, which is among the highest, albeit not certified, reported to date organic for BHJ solar cells.^[8] Note that the calculated J_{SC} from the EQE spectrum for this particular cell (18.94 mA cm^{-2}) agrees well with the measured J_{SC} from the J - V curve (19 mA cm^{-2}). It is also interesting to note that only in the case of P3HT:ICBA cells a small improvement in the V_{OC} , from 0.844 to 0.854 V, is observed suggesting that only in this particular blend the V_{OC} is somewhat limited by the ETL. On the basis of the results presented so far it is clear that insertion of the ultra-thin layer of In₂O₃ between the ITO and ZnO has a consistent positive impact on the operating characteristics of all organic BHJ cells investigated.

6. Bilayer In₂O₃/ZnO ETL-Based PbS Colloidal Quantum Dot Solar Cells

We sought to extend the application gamut of the bilayer ITO/In₂O₃/ZnO(s-g) ETLs beyond the organic BHJ solar cell

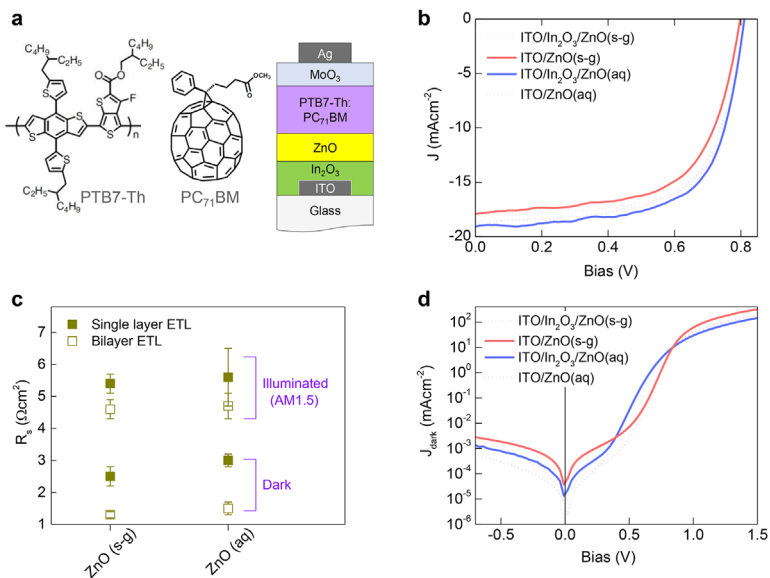


Figure 5. a) Chemical structure of the donor polymer PTB7-Th and acceptor small-molecule PC₇₁BM together with the inverted cell architecture employed. b) *J*-*V* characteristics of PTB7-Th:PCBM solar cells employing the single layer and bilayer ETLs measured under simulated solar illumination (100 mW cm⁻², air mass 1.5 G). c) Comparison of the series resistance (*R*_s) for single layer and bilayer ETL-based solar cells calculated from both the illuminated (b) and dark *J*-*V* curves shown in (d).

platform. Toward this end, we fabricated solar cells that employ lead sulfide (PbS) CQDs as the light absorbing layer. CQD solar cells form another major category of potentially cost-effective, solution-processable thin-film PV owing to their strong absorption in the infrared and, therefore, better harvesting of the solar spectrum.^[61–63] CQD solar cells typically employ a thick (100–150) ZnO nanoparticle ETL in order to achieve sufficient depletion within the active CQD layer.^[64,65] To test whether a much thinner ETL is possible using the bilayer In₂O₃/ZnO, we fabricated CQD solar cells employing the same bilayer ETL as used for our organic BHJ devices (thickness of ≈30–35 nm). To fabricate the active layer, initially insulating, oleic-acid (OA) capped CQDs were made to undergo a ligand exchange in the solution phase with lead halides (PbX₂; X = I, Br) leading to a conducting, dense ink of electronically coupled halide-capped (PbX₂-PbS) CQDs dispersed in the butylamine (BTA) solvent.^[64,65] This was used to form an absorber layer, in a single-step, by coating on top of the bi-layered ETL-covered substrate leading to a planar depleted heterojunction.^[21] To further

enhance the extraction and egress of charge carriers to the respective electrodes, a 1,2-ethanedithiol (EDT) ligand capped PbS CQD layer was deposited as the hole transporter atop the absorber, resulting in an n-i-p architecture device.

Figure 7a shows the *J*-*V* curve of the best performing cell (8.2% PCE) based on the bilayer In₂O₃/ZnO(s-g) ETL, with the schematic of the solar cell architecture shown in the inset. The average PCE over 15 devices was 7.8 (±0.2)% with high reproducibility (Figure 7b), which is significantly higher than the values obtained from the control devices employing a similarly thin (≈30 nm) single layer ZnO(s-g) ETL (mean PCE of 7.1 [±0.4]%). While this is still lower than the PCE obtained from control cells using a thick (≈150 nm) nanoparticle ZnO ETL (average PCE of 9.2 (±0.3)%, Figure S6, Supporting Information), further work on optimizing the bilayer ETL-based cell architecture and understanding the device physics is ongoing and will be addressed in future reports.

7. Conclusion

In conclusion, we have demonstrated high-efficiency organic BHJ and inorganic quantum dot solar cells based on In₂O₃/ZnO heterojunction electron-transport layers processed both from an aqueous and a sol-gel route. HRTEM and AFM morphological characterization confirmed the presence of a chemically sharp In₂O₃/ZnO heterointerface on top of ITO electrodes, that is characterized by a reduced surface roughness as compared to reference ITO/ZnO electrodes. Kelvin Probe measurements indicate a decrease in the work function of the bilayer structure compared to the single layer structure, an effect most likely attributed to electron accumulation at the sharp In₂O₃/ZnO heterointerface. Correspondingly, the performance of organic BHJ solar cells based on PTB7-Th:PC₇₀BM was significantly improved when the single layer ZnO was replaced with bilayer In₂O₃/ZnO as the ETL. Obtained devices exhibited reduced series resistance, higher FF and PCE values of >10%. The universality of the bilayer In₂O₃/ZnO heterointerface ETL structure proposed was further demonstrated by its use in organic BHJ solar cells based on a range of different organic donor-acceptor systems. Improvements in performance with the bilayer In₂O₃/ZnO over the

Table 2. Summary of the operating parameters under illumination for PTB7-Th:PC₇₀BM solar cells based on different metal oxide ETLs.

ETL ^{a)}	<i>J</i> _{sc} [mA cm ⁻²]	<i>V</i> _{oc} [V]	FF	PCE [%]	<i>R</i> _{s,l} [Ω cm ²]	<i>R</i> _{s,d} [Ω cm ²] ^{b)}	<i>R</i> _{sh} [Ω cm ²]
ZnO (ac)	17.7 ± 0.4	0.795 ± 0.003	0.63 ± 0.01	8.9 ± 0.2	5.4 ± 0.3	2.5 ± 0.3	797 ± 42
In ₂ O ₃ /ZnO(ac)	17.9 ± 0.3	0.803 ± 0.004	0.67 ± 0.01	9.6 ± 0.3	4.6 ± 0.3	1.3 ± 0.1	704 ± 210
ZnO (NP)	17.9 ± 0.5	0.814 ± 0.001	0.64 ± 0.02	9.4 ± 0.3	5.6 ± 0.9	3.0 ± 0.2	732 ± 180
In ₂ O ₃ /ZnO(NP)	18.3 ± 0.8	0.812 ± 0.002	0.66 ± 0.005	9.8 ± 0.4	4.7 ± 0.4	1.5 ± 0.2	806 ± 410

^{a)} Mean values obtained from at least 15 individual cells; the standard deviation around the mean is shown.

^{b)} Series resistance calculated from the dark *J*-*V* curves of the same cells.

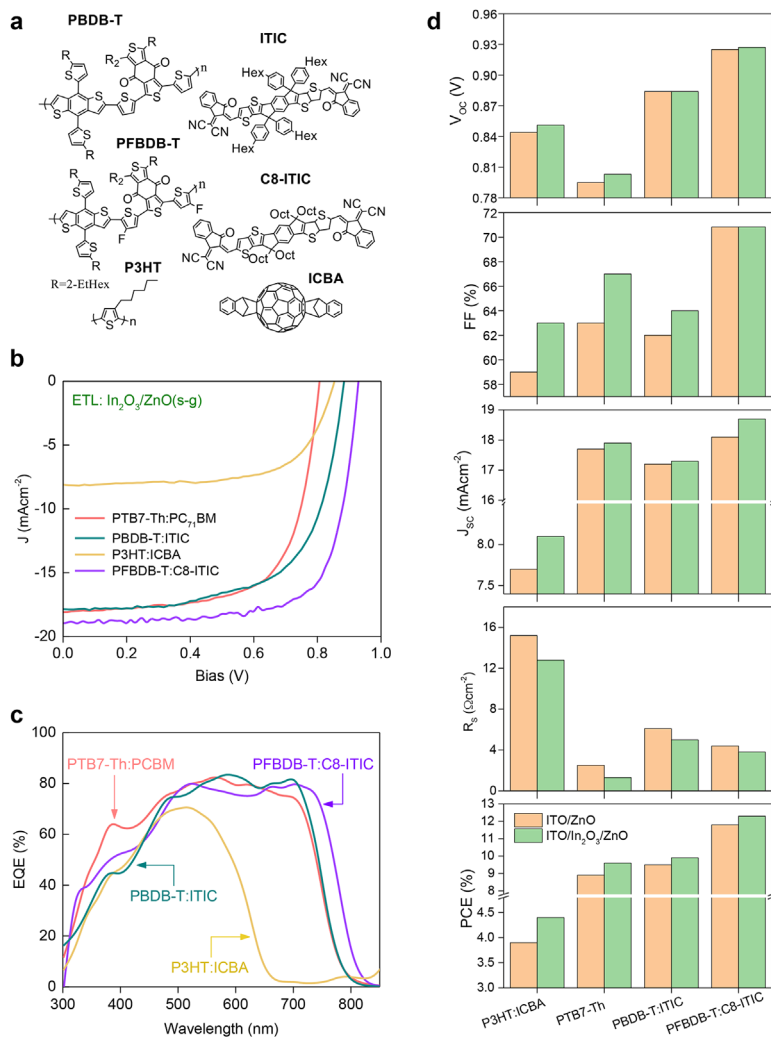


Figure 6. a) Chemical structures of the active materials used in the OPV devices. b) J - V characteristics of the various OPV cells employing $\text{In}_2\text{O}_3/\text{ZnO}(\text{s-g})$ as the ETL, and (c) corresponding EQE spectra. The integrated J_{sc} values of 17.8, 18.3, 9.1, and 17.6 mA cm^{-2} for PTB7-Th:PC₇₁BM, PFBDB-T:8C-ITIC, P3HT:ICBA, and PBDB-T:ITIC, respectively, agree well with the corresponding J_{sc} from J - V measurements. d) Comparison of OPV parameters between cells employing single layer ZnO and bilayer $\text{In}_2\text{O}_3/\text{ZnO}$ ETLs.

single layer ZnO ETL architecture was observed with all the blends tested, for which a maximum PCE of 12.8% was achieved for PFBDB-T:8C-ITIC cells. Finally, the bilayer ETL concept was also applied to inorganic PbS CQDs, where thin 35 nm bilayer

ETL films yielded a comparable performance to the thick (≈ 150 nm) ZnO nanoparticle ETL-based reference devices.

8. Experimental Section

Materials and Solutions: ZnO (s-g) solutions were prepared by dissolving zinc acetate (99.99%, Sigma-Aldrich) at 110 mg mL^{-1} in 2-methoxyethanol (anhydrous, 99.8%, Sigma-Aldrich) containing 3% ethanolamine (99.5%, Sigma-Aldrich) overnight, and ZnO (aq) precursor solutions were prepared by dissolving zinc oxide (ZnO, 99.99%, Sigma-Aldrich) nanoparticles in aqueous ammonium hydroxide solution (NH_4OH , 50% v/v aqn. soln., Alfar Aesar) at 10 mg mL^{-1} under constant stirring at room temperature. In_2O_3 precursor solutions were prepared by dissolving 20 mg mL^{-1} indium nitrate hydrate ($\text{In}(\text{NO}_3)_3 \cdot x\text{H}_2\text{O}$, 99.99%, Indium Corporation) in 2-methoxyethanol (99.8%, Sigma-Aldrich).

PTB7-Th (weight-average molecular weight $>40\,000$, polydispersity index 1.8-2.0) was purchased from Solenne. Poly[(2,6-(4,8-bis(5-(2-ethylhexyl)thiophen-2-yl)-benzo[1,2-*b*:4,5-*b'*]dithiophene))-alt-(5,5-(1',3'-di-2-thienyl-5',7'-bis(2-ethylhexyl)benzo[1',2'-*c*:4',5'-*c'*]dithiophene-4,8-dione)] (PBDB-T)^[57] (M_n 23 000; M_w 48 300 g mol^{-1}), 3,9-bis(2-methylene-(3-(1,1-dicyanomethylene)indanone)-5,5,11,11-tetrakis(4-hexylphenyl)-dithieno[2,3-*d*:2',3'-*d'*]-s-indaceno[1,2-*b*:5,6-*b'*]dithiophene (ITIC),^[60] {(2Z)-2-[(8-((E)-[1-(Dicyanomethylidene)-3-oxo-1,3-dihydro-2H-inden-2-ylidene]methyl)-6,6,12,12-tetraoctyl-6,12-dihydrothieno[3,2-*j*]thieno[2',3'':4',5']thieno[2',3':5,6]-sindaceno[2,1-*d*]thiophen-2-yl)methylidene]-3-oxo-2,3-dihydro-1H-inden-1-ylidene]propanedinitrile (8C-ITIC)^[8] and poly[(2,6-(4,8-bis(5-(2-ethylhexyl)thiophen-2-yl)-benzo[1,2-*b*:4,5-*b'*]dithiophene))-alt-(5,5-(1',3'-bis(4-fluorothiophen-2-yl)-5',7'-bis(2-ethylhexyl)benzo[1',2'-*c*:4',5'-*c'*]) (PFBDB-T) (M_n 26 000; M_w 67 600 g mol^{-1})^[8] were prepared by the reported procedures. PC₇₁BM and ICBA (both $>99\%$ purity) were purchased from Solenne, respectively. The polymer molecular weights were determined using an Agilent Technologies 1200 series GPC running in chlorobenzene at 80°C , using two PL mixed B columns in series, and calibrated against narrow polydispersity polystyrene standards.

PTB7-Th:PC₇₁BM (1:1.5 by weight) solutions were prepared by dissolving the materials at 25 mg mL^{-1} in 97 vol% chlorobenzene (CB) and 3 vol% 1,8-diiodooctane (DIO) at 70 degrees. PBDB-T:ITIC (1:1 by weight) solutions were prepared by dissolving the materials at 20 mg mL^{-1} in 99.5 vol% chlorobenzene (CB) and 0.5 vol% 1,8-diiodooctane (DIO) at 50 degrees. PFBDB-T:8C-ITIC (1:1.25 by weight) solutions were prepared by dissolving the materials at 20 mg mL^{-1} in chlorobenzene (CB) at 50 degrees. P3HT:

Table 3. Summary of the extracted operating parameters for solar cells with various active layer compositions employing bilayer $\text{In}_2\text{O}_3/\text{ZnO}$ ETLs.

Active layer ^{a)}	ETL	J_{sc} [mA cm^{-2}]	V_{oc} [V]	FF	PCE [%]	R_s [Ωcm^2]
P3HT:ICBA	$\text{In}_2\text{O}_3/\text{ZnO}$	8.1 (± 0.1)	0.851 (± 0.006)	0.63 (± 0.03)	4.4 (± 0.3)	12.8 (± 2.0)
PBDB-T:ITIC	$\text{In}_2\text{O}_3/\text{ZnO}$	17.3 (± 0.3)	0.884 (± 0.005)	0.64 (± 0.01)	9.9 (± 0.4)	5 (± 0.4)
PFBDB-T:8C-ITIC	$\text{In}_2\text{O}_3/\text{ZnO}$	18.7 (± 0.5)	0.927 (± 0.002)	0.71 (± 0.01)	12.3 (± 0.4)	3.8 (± 0.3)
PFBDB-T:8C-ITIC ^{b)}	$\text{In}_2\text{O}_3/\text{ZnO}$	19.0 ^{b)}	0.93 ^{b)}	0.73 ^{b)}	12.8 ^{b)}	3.8 ^{b)}

^{a)} Mean values obtained from at least 15 individual cells; the standard deviation around the mean is given in brackets.

^{b)} Values obtained for the best performing PFBDB-T:8C-ITIC device.

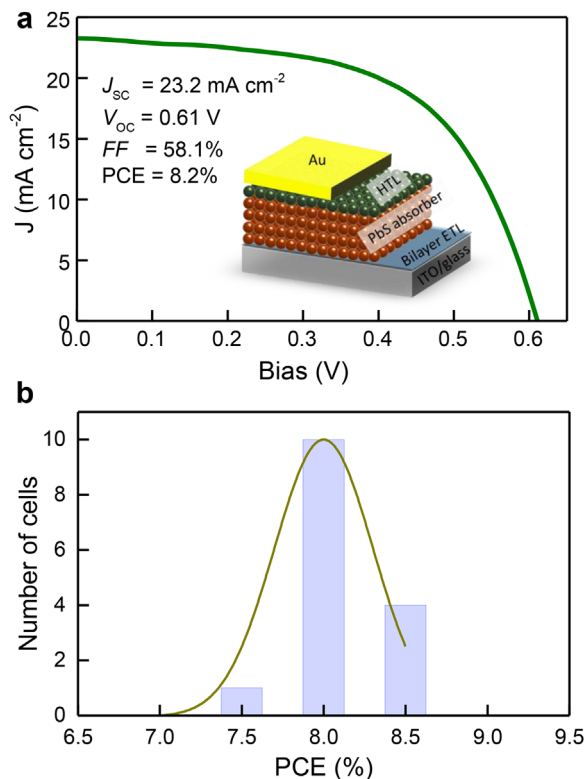


Figure 7. a) *J*-*V* characteristics for PbS quantum dot solar cells employing a bilayer In₂O₃/ZnO ETL, with the device parameters obtained for the best device shown. The device architecture used is shown in the inset. b) Spread of power conversion efficiencies obtained for ten individual cells.

ICBA (1:1 by weight) solutions were prepared by dissolving the materials at 40 mg mL⁻¹ in dichlorobenzene (DCB).

Metal Oxide Thin-Film Deposition: Substrates were cleaned using solvents prior to thin-film deposition by a sequential ultrasonication procedure: an aqueous solution of Decon 90, deionized water, acetone, and isopropanol. After cleaning the substrates were dried in a nitrogen flow, and were UV-ozone treated for 15 min. For single layer thin films, ZnO (aq) and ZnO (s-g) precursor solutions were spin cast at 4000 and 2000 rpm, and were annealed at 160 and 200 degrees, respectively, for 1 h. Bilayer thin films were obtained by spin coating the indium nitrate precursor solution at 6000 rpm, followed by annealing at 200 °C for 1 h and UV-Ozone treatment for 10 min, followed by the deposition of the ZnO. All metal oxide depositions were carried out in air.

Ultraviolet-Visible-Near-Infrared (UV-Vis-NIR) spectroscopy: The samples were measured using a Shimadzu UV-2600 spectrophotometer equipped with an ISR-2600Plus integrating sphere, and transmission spectra were obtained in the region of 300–1200 nm.

Atomic Force Microscopy (AFM): The surface morphology was studied using an Agilent 5500 atomic force microscope in tapping mode in air. The approximate resonant frequency of the cantilever was 270 kHz with a force constant of 40 N m⁻¹.

Transmission Electron Microscopy: The lamella of the ZnO/In₂O₃ bilayer structure on the ITO-patterned glass substrate for the HRTEM and EDS analysis was prepared in a scanning electron microscope (Helios 400s, FEI) equipped with a nanomanipulator (omniprobe, AutoProbe300) with the help of a focused ion beam (FIB). In order to protect the layers of interest carbon was deposited under electron and ion beams to reach a thickness of ca. 2 μm. Ga ion beam (30 kV, 21 nA) was used first to mill the

bulk and then (30 kV, 9 nA) to cut the lamella, which was attached to a copper grid in accordance with the lift-out method. The lamella thickness was reduced with the ion beam (30 kV, 93 pA) to less than 90 nm and then cleaned from possible contamination (5 kV, 28 pA). A transmission electron microscope (Titan 80-300, FEI) was used to obtain the HRTEM images at 300 kV operating voltage. The EDS line scan was acquired in the same microscope in a scanning TEM (STEM) mode with the Gatan Imaging Filter (GIF) Quantum 966.

Kelvin Probe (KP) Measurements: The Fermi levels of the metal oxide thin films were determined using KP contact potential difference measurement with a KP Technology SKP5050 Scanning Kelvin Probe in a nitrogen environment at room temperature. The Fermi level was calculated with respect to the work function of a polished silver reference sample.

Transistor Fabrication and Characterization: Bottom-gate top-contact transistors were fabricated by spin coating the metal oxide precursor solutions onto highly doped Si (Si⁺⁺) substrates with a 400 nm thermally grown SiO₂ layer acting as the common gate and dielectric using the above described method. Following the thin film deposition, 40 nm-thick Al source/drain contacts were deposited through a shadow mask *via* thermal evaporation in high vacuum (<10⁻⁵ mbar), to result in transistors with channel length and width of 100 and 1000 μm, respectively.

Photovoltaic Cell Fabrication and Characterization: Inverted organic solar cells were fabricated by the deposition of the single or bilayer ZnO thin films on ITO, followed by the deposition of the active layers in a nitrogen atmosphere. PTB7-Th:PC₇₁BM active layers were produced by the spin coating of the solution at 3000 rpm, followed by a methanol wash at 4000 rpm. For P3HT:ICBA, the solution was spin cast at 1500 rpm, followed by annealing at 150 degrees for 10 min. PBDB-T:ITIC and PFBDB-T:8C-ITIC active layers were both fabricated by spin casting of the solutions at 2000 rpm, and PBDB-T:ITIC films were annealed at 150 degrees for 10 min, following literature procedures.^[8] Photovoltaic cells were completed by the evaporation of 10/80 nm MoO₃/Ag cathodes through shadow masks with an aperture of 0.05 cm², in a high vacuum. *J*-*V* characteristics were measured using a Keithley 2400 source-meter. The cells were illuminated by an AM1.5 xenon lamp solar simulator (Oriental Instruments) under 1 sun intensity, which was monitored using a calibrated Si reference photodiode. The active area of the cells under illumination was defined by 0.04 cm² masks. All devices were stored in dark prior to characterization and were measured in a nitrogen-filled chamber.

CQD Synthesis: CQD synthesis of oleic-acid (OA) capped PbS CQDs (exciton absorption at 881 nm) was carried out following a recent literature report.^[64]

Device Fabrication: Following deposition of the ETL, the solution-phase ligand exchanged ink of PbX₂-PbS CQDs (200 mg mL⁻¹ solution in butylamine) was spincoated on the ETL-covered substrate (2500 rpm, 15 s). This was followed by deposition of the EDT-PbS CQD HTL which was done via the layer-by-layer (LbL) method,^[66,67] as explained here: OA-capped CQDs were spincoated (2500 rpm, 15 s) followed by ligand exchange with 0.01% (v:v) EDT solution in acetonitrile (ACN) solvent (30 s wait). The exchanged film was rinsed with ACN. This was repeated twice. Finally, Au electrodes (80 nm) were thermally evaporated using an Angstrom evaporator.

Supporting Information

Supporting Information is available from the Wiley Online Library or from the author.

Acknowledgment

The work reported here was supported by the King Abdullah University of Science and Technology (KAUST).

Conflict of Interest

The authors declare no conflict of interest.

Keywords

colloidal quantum dot solar cells, electron transport layers, indium oxide, organic solar cells, zinc oxide

Received: March 15, 2018

Revised: March 23, 2018

Published online: April 25, 2018

- [1] M. M. Voigt, R. C. I. Mackenzie, C. P. Yau, P. Atienzar, J. Dane, P. E. Keivanidis, D. D. C. Bradley, J. Nelson, *Sol. Energy Mater. Sol. Cells* **2011**, 95, 731.
- [2] F. C. Krebs, *Org. Electron.* **2009**, 10, 761.
- [3] F. C. Krebs, *Sol. Energy Mater. Sol. Cells* **2009**, 93, 1636.
- [4] Y. Liu, J. Zhao, Z. Li, C. Mu, W. Ma, H. Hu, K. Jiang, H. Lin, H. Ade, H. Yan, *Nat. Commun.* **2014**, 5, 5293.
- [5] S. Nam, J. Seo, S. Woo, W. H. Kim, H. Kim, D. D. C. Bradley, Y. Kim, *Nat. Comms.* **2015**, 6, 8929.
- [6] N. Wijeyasinghe, A. Regoutz, F. Eisner, T. Du, L. Tsetseris, Y.-H. Lin, H. Faber, P. Pattanasattayavong, J. Li, F. Yan, M. A. McLachlan, D. J. Payne, M. Heeney, T. D. Anthopoulos, *Adv. Funct. Mater.* **2017**, 27, 1701818.
- [7] Y. Cui, H. Yao, B. Gao, Y. Qin, S. Zhang, B. Yang, C. He, B. Xu, J. Hou, *J. Am. Chem. Soc.* **2017**, 139, 7302.
- [8] Z. Fei, F. D. Eisner, X. Jiao, M. Azzouzi, J. A. Röhr, Y. Han, M. Shahid, A. S. R. Chesman, C. D. Easton, C. R. McNeill, T. D. Anthopoulos, J. Nelson, M. Heeney, *Adv. Mater.* **2018**, 30, 1705209.
- [9] W. Zhao, S. Li, H. Yao, S. Zhang, Y. Zhang, B. Yang, J. Hou, *J. Am. Chem. Soc.* **2017**, 139, 7148.
- [10] P. Pattanasattayavong, A. D. Mottram, F. Yan, T. D. Anthopoulos, *Adv. Funct. Mater.* **2015**, 25, 6802.
- [11] N. Yaacobi-Gross, N. D. Treat, P. Pattanasattayavong, H. Faber, A. K. Perumal, N. Stingelin, D. D. C. Bradley, P. N. Stavrinou, M. Heeney, T. D. Anthopoulos, *Adv. Energy Mater.* **2015**, 5, 1401529.
- [12] N. D. Treat, N. Yaacobi-Gross, H. Faber, A. K. Perumal, D. D. C. Bradley, N. Stingelin, T. D. Anthopoulos, *Appl. Phys. Lett.* **2015**, 107, 013301.
- [13] J. Huang, Z. Yin, Q. Zheng, *Energy Environ. Sci.* **2011**, 4, 3861.
- [14] D. Khim, Y.-H. Lin, S. Nam, H. Faber, K. Tetzner, R. Li, Q. Zhang, J. Li, X. Zhang, T. D. Anthopoulos, *Adv. Mater.* **2017**, 29, 1605837.
- [15] A. K. K. Kyaw, X. W. Sun, C. Y. Jiang, G. Q. Lo, D. W. Zhao, D. L. Kwong, *Appl. Phys. Lett.* **2008**, 93, 221107.
- [16] Z. Lin, J. Chang, C. Zhang, J. Zhang, J. Wu, Y. Hao, *J. Mater. Chem. C* **2016**, 4, 6169.
- [17] S. Woo, W. Hyun Kim, H. Kim, Y. Yi, H.-K. Lyu, Y. Kim, *Adv. Energy Mater.* **2014**, 4, 1301692.
- [18] T.-H. Lai, S.-W. Tsang, J. R. Manders, S. Chen, F. So, *Mater. Today* **2013**, 16, 424.
- [19] L.-M. Chen, Z. Xu, Z. Hong, Y. Yang, *J. Mater. Chem.* **2010**, 20, 2575.
- [20] R. Steim, F. R. Kogler, C. J. Brabec, *J. Mater. Chem.* **2010**, 20, 2499.
- [21] C.-H. M. Chuang, P. R. Brown, V. Bulović, M. G. Bawendi, *Nat. Mater.* **2014**, 13, 796.
- [22] W. Deng, X. Liang, P. S. Kubiak, P. J. Cameron, *Adv. Energy Mater.* **2018**, 8, 1701544.
- [23] F. Hermerschmidt, A. Savva, E. Georgiou, S. M. Tuladhar, J. R. Durrant, I. McCulloch, D. D. C. Bradley, C. J. Brabec, J. Nelson, S. A. Choulis, *ACS Appl. Mater. Interfaces* **2017**, 9, 14136.
- [24] S. M. Tuladhar, M. Azzouzi, F. Delval, J. Yao, A. A. Y. Guilbert, T. Kirchartz, N. F. Montcada, R. Dominguez, F. Langa, E. Palomares, J. Nelson, *ACS Energy Lett.* **2016**, 1, 302.
- [25] C. Waldauf, M. Morana, P. Denk, P. Schilinsky, K. Coakley, S. A. Choulis, C. J. Brabec, *Appl. Phys. Lett.* **2006**, 89, 233517.
- [26] S. K. Hau, H.-L. Yip, A. K. Y. Jen, *Polym. Rev.* **2010**, 50, 474.
- [27] Z. Yin, J. Wei, Q. Zheng, *Adv. Sci.* **2016**, 3, 1500362.
- [28] Y. Sun, J. H. Seo, C. J. Takacs, J. Seifert, A. J. Heeger, *Adv. Mater.* **2011**, 23, 1679.
- [29] S. Bai, Z. Wu, X. Xu, Y. Jin, B. Sun, X. Guo, S. He, X. Wang, Z. Ye, H. Wei, X. Han, W. Ma, *Appl. Phys. Lett.* **2012**, 100, 203906.
- [30] Y.-H. Lin, H. Faber, K. Zhao, Q. Wang, A. Amassian, M. McLachlan, T. D. Anthopoulos, *Adv. Mater.* **2013**, 25, 4340.
- [31] H. Kim, C. M. Gilmore, J. S. Horwitz, A. Piqué, H. Murata, G. P. Kushto, R. Schlaf, Z. H. Kafafi, D. B. Chrisey, *Appl. Phys. Lett.* **2000**, 76, 259.
- [32] X. Liu, X. Li, Y. Li, C. Song, L. Zhu, W. Zhang, H.-Q. Wang, J. Fang, *Adv. Mater.* **2016**, 28, 7405.
- [33] G. B. Murdoch, S. Hinds, E. H. Sargent, S. W. Tsang, L. Mordoukhovski, Z. H. Lu, *Appl. Phys. Lett.* **2009**, 94, 213301.
- [34] K. Schulze, B. Maennig, K. Leo, Y. Tomita, C. May, J. Hüpkes, E. Brier, E. Reinold, P. Bäuerle, *Appl. Phys. Lett.* **2007**, 91, 073521.
- [35] T. Stubhan, H. Oh, L. Pinna, J. Krantz, I. Litzov, C. J. Brabec, *Org. Electron.* **2011**, 12, 1539.
- [36] F. Z. Bedia, A. Bedia, M. Aillerie, N. Maloufi, B. Benyoucef, *Energy Procedia* **2015**, 74, 539.
- [37] S.-H. Liao, H.-J. Jhuo, P.-N. Yeh, Y.-S. Cheng, Y.-L. Li, Y.-H. Lee, S. Sharma, S.-A. Chen, *Sci. Rep.* **2014**, 4, 6813.
- [38] B. R. Lee, E. D. Jung, Y. S. Nam, M. Jung, J. S. Park, S. Lee, H. Choi, S.-J. Ko, N. R. Shin, Y.-K. Kim, S. O. Kim, J. Y. Kim, H.-J. Shin, S. Cho, M. H. Song, *Adv. Mater.* **2014**, 26, 494.
- [39] X. Guan, K. Zhang, F. Huang, G. C. Bazan, Y. Cao, *Adv. Funct. Mater.* **2012**, 22, 2846.
- [40] S.-I. Na, S.-H. Oh, S.-S. Kim, D.-Y. Kim, *Org. Electron.* **2009**, 10, 496.
- [41] C. Duan, K. Zhang, C. Zhong, F. Huang, Y. Cao, *Chem. Soc. Rev.* **2013**, 42, 9071.
- [42] T. Yang, M. Wang, C. Duan, X. Hu, L. Huang, J. Peng, F. Huang, X. Gong, *Energy Environ. Sci.* **2012**, 5, 8208.
- [43] Y. Zhou, C. Fuentes-Hernandez, J. Shim, J. Meyer, A. J. Giordano, H. Li, P. Winget, T. Papadopoulos, H. Cheun, J. Kim, M. Fenoll, A. Dindar, W. Haske, E. Najafabadi, T. M. Khan, H. Sojoudi, S. Barlow, S. Graham, J.-L. Brédas, S. R. Marder, A. Kahn, B. Kippelen, *Science* **2012**, 336, 327.
- [44] H. Kang, S. Hong, J. Lee, K. Lee, *Adv. Mater.* **2012**, 24, 3005.
- [45] Y. Zhou, C. Fuentes-Hernandez, J. W. Shim, T. M. Khan, B. Kippelen, *Energy Environ. Sci.* **2012**, 5, 9827.
- [46] L. K. Jagadamma, M. Al-Senani, A. El-Labban, I. Gereige, G. O. Ngongang Ndjawa, J. C. D. Faria, T. Kim, K. Zhao, F. Cruciani, D. H. Anjum, M. A. McLachlan, P. M. Beaujuge, A. Amassian, *Adv. Energy Mater.* **2015**, 5, 1500204.
- [47] S. Pradhan, A. Stavrinadis, S. Gupta, G. Konstantatos, *ACS Appl. Mater. Interfaces* **2017**, 9, 27390.
- [48] J. G. Labram, Y.-H. Lin, T. D. Anthopoulos, *Small* **2015**, 11, 5472.
- [49] J. G. Labram, Y.-H. Lin, K. Zhao, R. Li, S. R. Thomas, J. Semple, M. Androulidaki, L. Sygellou, M. McLachlan, E. Stratakis, A. Amassian, T. D. Anthopoulos, *Adv. Funct. Mater.* **2015**, 25, 1727.
- [50] Y.-H. Lin, H. Faber, J. G. Labram, E. Stratakis, L. Sygellou, E. Kymakis, N. A. Hastas, R. Li, K. Zhao, A. Amassian, N. D. Treat, M. McLachlan, T. D. Anthopoulos, *Adv. Sci.* **2015**, 2, 1500058.
- [51] K. Tetzner, I. Isakov, A. Regoutz, D. J. Payne, T. D. Anthopoulos, *J. Mater. Chem. C* **2017**, 5, 59.
- [52] Y. Peng, N. Yaacobi-Gross, A. K. Perumal, H. A. Faber, G. Vourlias, P. A. Patsalas, D. D. C. Bradley, Z. He, T. D. Anthopoulos, *Appl. Phys. Lett.* **2015**, 106, 243302.

- [53] M. Thirumoorthi, J. Thomas Joseph Prakash, *J. Asian Ceramic Soc.* **2016**, *4*, 124.
- [54] Z. Liang, Q. Zhang, O. Wiranwetchayan, J. Xi, Z. Yang, K. Park, C. Li, G. Cao, *Adv. Funct. Mater.* **2012**, *22*, 2194.
- [55] Z. Ma, Z. Tang, E. Wang, M. R. Andersson, O. Inganäs, F. Zhang, *J. Phys. Chem. C* **2012**, *116*, 24462.
- [56] H. Faber, S. Das, Y.-H. Lin, N. Pliatsikas, K. Zhao, T. Kehagias, G. Dimitrakopoulos, A. Amassian, P. A. Patsalas, T. D. Anthopoulos, *Sci. Adv.* **2017**, *3*, e1602640.
- [57] S.-H. Liao, H.-J. Jhuo, Y.-S. Cheng, S.-A. Chen, *Adv. Mater.* **2013**, *25*, 4766.
- [58] M. M. Wienk, J. M. Kroon, W. J. H. Verhees, J. Knol, J. C. Hummelen, P. A. van Hal, R. A. J. Janssen, *Angew. Chem.* **2003**, *115*, 3493.
- [59] D. Qian, L. Ye, M. Zhang, Y. Liang, L. Li, Y. Huang, X. Guo, S. Zhang, Z. a. Tan, J. Hou, *Macromolecules* **2012**, *45*, 9611.
- [60] Y. Lin, J. Wang, Z.-G. Zhang, H. Bai, Y. Li, D. Zhu, X. Zhan, *Adv. Mater.* **2015**, *27*, 1170.
- [61] E. H. Sargent, *Nat. Photon.* **2012**, *6*, 133.
- [62] C. R. Kagan, E. Lifshitz, E. H. Sargent, D. V. Talapin, *Science* **2016**, *353*, 885.
- [63] S. A. McDonald, G. Konstantatos, S. Zhang, P. W. Cyr, E. J. D. Klem, L. Levina, E. H. Sargent, *Nat. Mater.* **2005**, *4*, 138.
- [64] M. Liu, O. Voznyy, R. Sabatini, F. P. Garcia de Arquer, R. Munir, A. H. Balawi, X. Lan, F. Fan, G. Walters, A. R. Kirmani, S. Hoogland, F. Laquai, A. Amassian, E. H. Sargent, *Nat. Mater.* **2017**, *16*, 258.
- [65] A. R. Kirmani, F. P. García de Arquer, J. Z. Fan, J. I. Khan, G. Walters, S. Hoogland, N. Wehbe, M. M. Said, S. Barlow, F. Laquai, S. R. Marder, E. H. Sargent, A. Amassian, *ACS Energy Lett.* **2017**, *2*, 1952.
- [66] G. H. Carey, K. W. Chou, B. Yan, A. R. Kirmani, A. Amassian, E. H. Sargent, *MRS Commun.* **2013**, *3*, 83.
- [67] A. R. Kirmani, G. H. Carey, M. Abdelsamie, B. Yan, D. Cha, L. R. Rollny, X. Cui, E. H. Sargent, A. Amassian, *Adv. Mater.* **2014**, *26*, 4717.